Geophysical Journal International

Geophys. J. Int. (2022) **229,** 900–914
Advance Access publication 2021 October 30
GJI Marine geosciences and applied geophysics

https://doi.org/10.1093/gji/ggab450

P-wave scattering by randomly distributed aligned cracks in fractal media

Rupeng Ma,[1] Jing Ba,[1] José M. Carcione[1,3] and Maxim Lebedev[2]

[1] *School of Earth Sciences and Engineering, Hohai University, Nanjing* 211100, *China. E-mail: jba@hhu.edu.cn; jingba@188.com*
[2] *WA School of Mines: Minerals, Energy and Chemical Engineering, Curtin University, Perth* 6151, *Australia*
[3] *National Institute of Oceanography and Applied Geophysics (OGS),* 34010 *Sgonico, Trieste, Italy*

Accepted 2021 October 26. Received 2021 September 18

SUMMARY

Seismic wave scattering dispersion and attenuation can be significant in cracked reservoirs. Many scattering models have been proposed, and the fractal (self-similar) features of the medium need to be further incorporated and analysed. We solve the *P*-wave scattering caused by fluid-saturated aligned cracks of finite thickness embedded in fractal media. The model is based on crack displacement discontinuities by using the Foldy approximation and representation theorem. The frequency dependence of velocity and attenuation are analysed as a function of the incidence angle and the crack and fluid properties. The results show that the crack density, thickness and radius can have a significant influence on the wave properties, as well as the fluid bulk modulus and saturation. The model requires three parameters to describe self-similar cracked media, and can be relevant in seismology, oil exploration and non-destructive testing of materials.

Key words: Fractals and multifractals; Acoustic properties; Seismic attenuation; Wave propagation; Wave scattering and diffraction.

1 INTRODUCTION

Attenuation and velocity dispersion associated with scattering can be significant when the length of the heterogeneities (i.e. inclusions and cracks) is comparable to or larger than the wavelength (e.g. Wu & Aki 1985a; Wu & Aki 1988; Sato *et al.* 2012). An analysis of the physics is useful to infer lithological properties, such as porosity, permeability and fluid saturation and type (e.g. Carcione 2014; Ba *et al.* 2017, 2019; Picotti *et al.* 2018; Zhang *et al.* 2020). The study has application in seismology, oil exploration and non-destructive testing of materials (e.g. Pulli 1984; Yamashita 1990; Kawahara 1992; Guo *et al.* 2009; Takahashi *et al.* 2014; Ba *et al.* 2019; Pang *et al.* 2019; Ma & Ba 2020).

Elastic wave scattering by cracks has been extensively studied theoretically, specifically in the isotropic case by a single penny-shaped crack (e.g. Mal 1970; Martin & Ursell 1981; Krenk *et al.* 1982; Keogh 1986). Scattering by a random distribution of dry cracks in an elastic solid has been investigated by using the non-interaction approximation (Foldy 1945) (e.g. Zhang & Achenbach 1991; Zhang & Gross 1993a,b; Murai *et al.* 1995; Murai 2007). Hudson (1981, 1986) studied the effect of aligned cracks in the long-wavelength limit and showed that the velocity depends on the crack density and aspect ratio.

The presence of fluids has been considered in many works (e.g. Garbin & Knopoff 1975; Kawahara 1992; Kawahara & Yamashita 1992; Gurevich *et al.* 1998; Fu *et al.* 2018, 2020; Guo *et al.* 2018, 2020; Song *et al.* 2019). Sabina *et al.* (1993) and Smyshlyaev *et al.* (1993) studied the attenuation effects using a dynamic self-consistent approach, but neglecting the fluid viscosity. Kawahara & Yamashita (1992) and Guo *et al.* (2018) considered aligned fluid-saturated slit cracks by taking into account the viscous friction between the fluid and crack surface, while Song *et al.* (2019) incorporated the hydraulic conduction inside the crack. However, these models assume oriented cracks of the same size. Thus, the crack size and distribution must be considered.

The crust and particularly hydrocarbon reservoirs contain cracks of different sizes. The pore or crack size distribution can be quantitatively described by a fractal geometry. This distribution can be described by a fractal dimension obtained from SEM (Scanning Electron Microscope) experiments (e.g. Katz & Thompson 1985; Krohn 1988a,b; Giri *et al.* 2013). Yu & Li (2001) assumed that the smallest pore diameter is at least two orders of magnitude smaller than the biggest one. Wu & Aki (1985b) considered the fractal nature of crustal inhomogeneities and found that scattering attenuation depends on their length scale. Yamashita (1990) found that the maximum crack radius ranges from 2 to 5 km by assuming a power-law distribution of radii on the basis of *SH* waves. Carcione *et al.* (2012) investigated the viscoelastic dissipation of an isotropic fractured medium by a finite-element method, considering fractal variations of the fracture compliances. Multiple scattering by

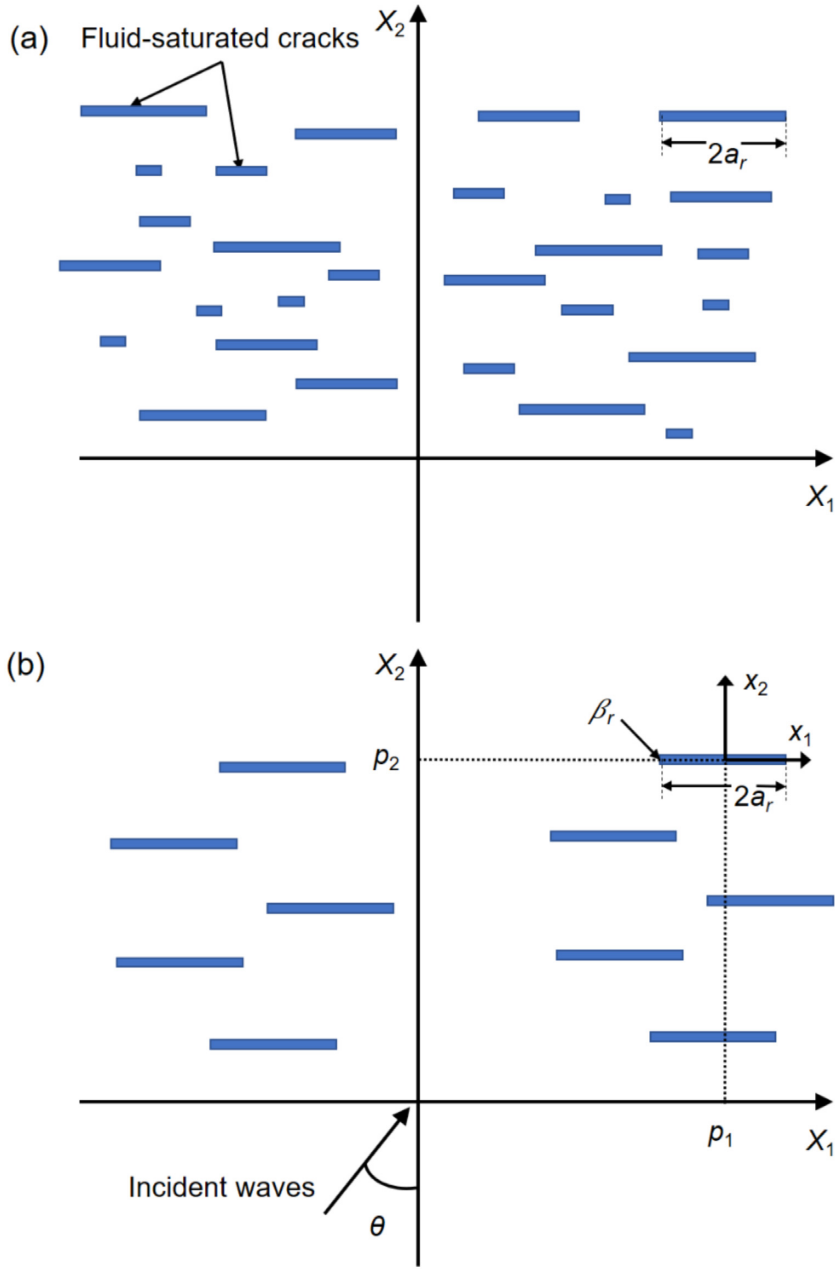

Figure 1. (a) Fluid-saturated medium with fractal (self-similar) crack sizes randomly and sparsely distributed along the X_1-axis, where the crack radius is in the range $[a_{\min}, a_{\max}]$. (b) The length and thickness of the cracks are $2a_r$ and β_r, respectively. A local coordinate system with origin at the centre (p_1, p_2) of the ith crack is considered, in which the x_1-axis is parallel to the crack strike. The incidence angle of the P wave is θ.

cracks and fractures with Gaussian or power-law distributions can be found in Lerche (1985), Ian Lerche & Petroy (1986) and Vlastos *et al.* (2007). The results show that attenuation can be used to characterize the fracture spatial scale.

We model cracked media characterized by fractality, assuming that the crack surfaces undergo viscous friction, but the interaction between different cracks (e.g. wave-induced fluid flow) is neglected by assuming a homogeneous and dilute distribution. We use the theories of Kawahara (1992) and Guo *et al.* (2018). The scattering dispersion and attenuation caused by fluid-saturated cracks are analysed by a specific example.

2 THEORY

2.1 Fractal (self-similar) cracked media

We assume that fluid-saturated cracks are randomly and sparsely distributed in isotropic elastic media, satisfying statistically self-similarity

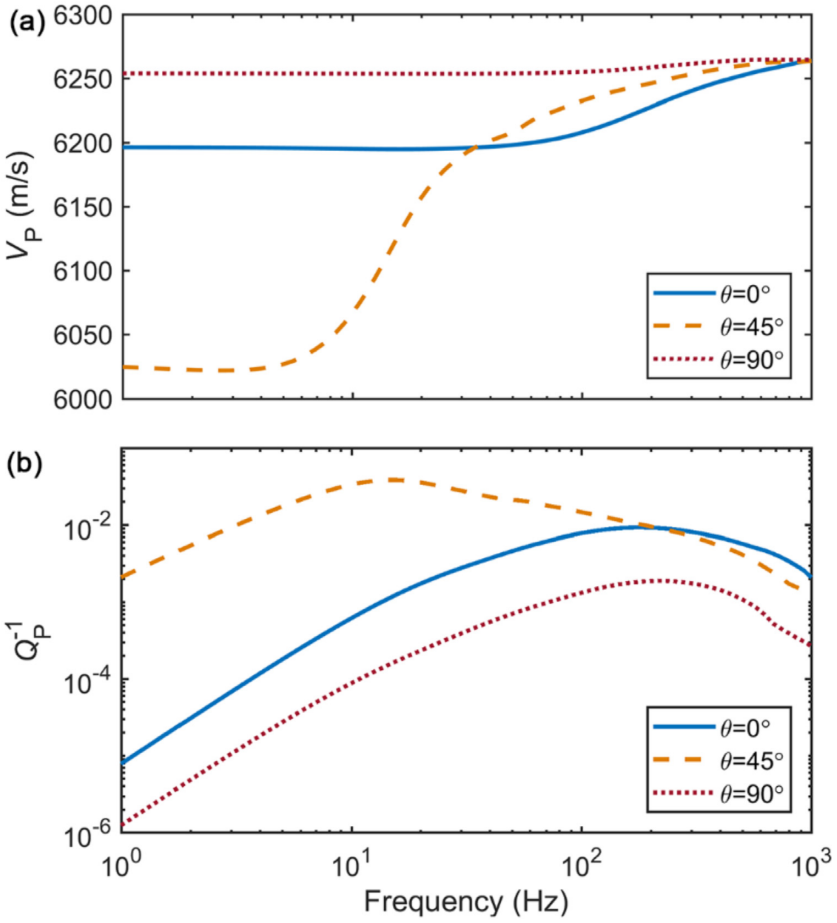

Figure 2. *P*-wave velocity (a) and dissipation factor (b) as a function of frequency and different incidence angles.

as shown in Fig. 1(a). The cumulative number of cracks follows the scaling law (Yu & Li 2001):

$$N(L \geq a_r) = \left(\frac{a_{max}}{a_r}\right)^{D_f}, \tag{1}$$

where a_r and a_{max} are the random and maximum crack radii, respectively, L is the length range of crack radii $[a_r, a_{max}]$, D_f is the fractal dimension in the range of 1–2 (2-D space) or 2–3 (3-D space). Then, the crack number in the range $[a_r, a_r + da_r]$ is

$$-\mathrm{d}N = D_f \left(\frac{a_r}{a_{max}}\right)^{-(D_f+1)} \mathrm{d}\left(\frac{a_r}{a_{max}}\right), \tag{2}$$

where the negative sign in the left-hand side denotes that the crack number decreases with the radius.

The total number N_t of cracks obtained from eq. (1) is

$$N_t(L \geq a_{min}) = \left(\frac{a_{max}}{a_{min}}\right)^{D_f}, \tag{3}$$

where a_{min} is the minimum crack radius.

The probability density function of the crack radius distribution can be obtained from eq. (2) divided by eq. (3) (Yu & Li 2001):

$$f(a_r) = D_f a_{min}^{D_f} a_r^{-(D_f+1)}, \tag{4}$$

where we have that $(a_{min}/a_{max})^{D_f} \cong 0$, namely, a_{min} is much smaller than a_{max}. In general, natural media satisfy $a_{min}/a_{max} < 10^{-2}$ (Yu *et al.* 2001).

2.2 Fluid-saturated aligned cracked media

P-wave scattering by a random distribution of aligned cracks in an infinite elastic medium has been previously studied (Kawahara & Yamashita 1992; Guo *et al.* 2018). 2-D aligned rectangular cracks of the same length and direction are randomly and uniformly distributed as shown in

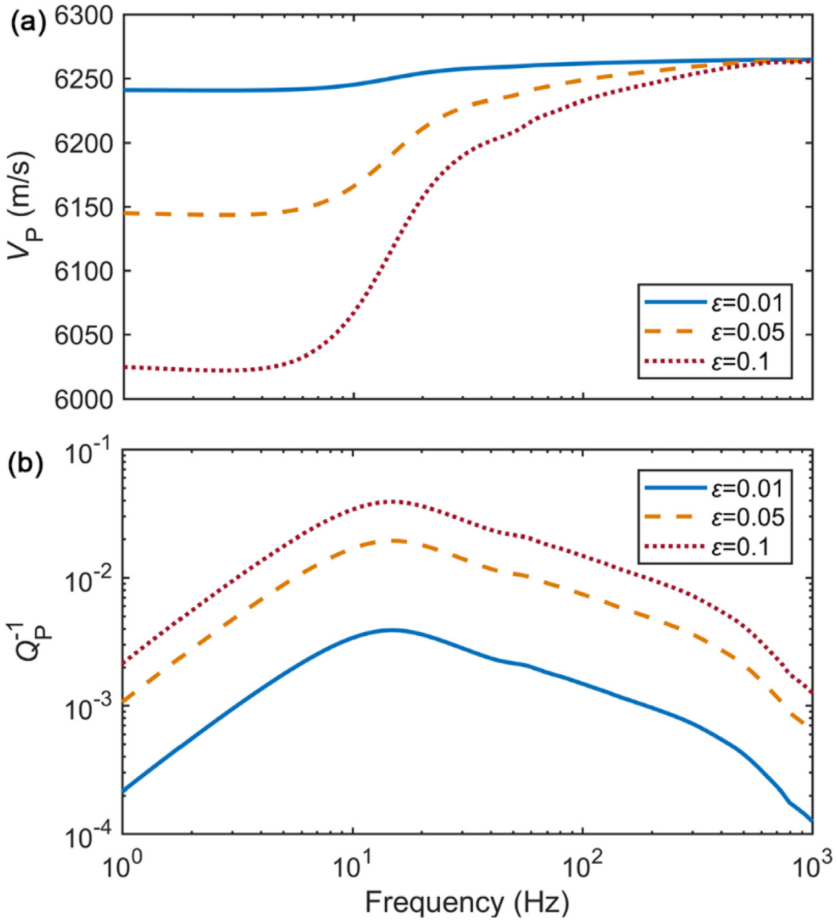

Figure 3. *P*-wave velocity (a) and dissipation factor (b) as a function of frequency for different crack densities ε at oblique incidence ($\theta = 45^\circ$).

Fig. 1(b). Cracks with a specific length $2a_r$ and thickness β_r, have their directions coinciding with the X_1-axis. The crack number density ν_r is the number per unit area of cracks with radius a_r, and plane *P* waves have an incidence angle θ.

For any incidence angle, the total displacement field is

$$\mathbf{u}^{\mathrm{T}} = \mathbf{u}^{\mathrm{I}} + \mathbf{u}, \tag{5}$$

where $\mathbf{u}^{\mathrm{I}}$ and $\mathbf{u}$ are the incident and scattered displacement field.

Since the cracks are randomly and sparsely distributed, the average displacement field can be obtained from the mean-wave formalism (Hudson 1980) and Foldy approximation (Foldy 1945):

$$\langle \mathbf{u}_{\mathrm{A}} \rangle = \mathbf{u}_{\mathrm{A}}^{0} + \nu_{\mathrm{r}} \int \mathbf{S}_{\mathrm{A}} \langle \mathbf{u}_{\mathbf{i}} \rangle \, \mathrm{d}\mathbf{r}_{\mathbf{i}}, \tag{6}$$

where $\mathbf{u}_{\mathrm{A}}^{0}$ is the incident wavefield, $\mathbf{S}_{\mathrm{A}}\langle \mathbf{u}_{\mathbf{i}} \rangle$ is the scattered wave induced by the *i*th crack, $\mathbf{r}_{\mathbf{i}}$ is the central location of the *i*th crack, and the subscript A denotes the observation point.

The incident time-harmonic plane *P* wave, with angular frequency ω, is

$$\mathbf{u}_{\mathrm{A}}^{0} = A_0 \mathrm{e}^{ik_{\mathrm{p}}X_1 \sin\theta + ik_{\mathrm{p}}X_2 \cos\theta} \left(\sin\theta, \cos\theta\right), \tag{7}$$

where A_0 is the displacement amplitude and k_{p} is the *P* wavenumber. The time dependence exp(-$i\omega t$) is omitted for brevity, and $\omega = 2\pi f$, where f is the frequency.

The ensemble average wavefield $\langle \mathbf{u}_{\mathrm{A}} \rangle$ is given by Kawahara (1992):

$$\langle \mathbf{u}_{\mathrm{A}} \rangle = A_1 \mathrm{e}^{ik_{\mathrm{p}}X_1 \sin\theta + i\left(k_{\mathrm{p}}\cos\theta + \kappa_{\mathrm{r}}\right)X_2} \left(\sin\theta, \cos\theta + \kappa_{\mathrm{r}}/k_{\mathrm{p}}\right), \tag{8}$$

where A_1 is the amplitude of the average wavefield, and κ_{r} is the parameter that determines the average attenuation. A local coordinate system (x_1, x_2) with origin (p_1, p_2) at the centre of the *i*th crack is considered (Fig. 1b). Thus, the average wavefield $\langle \mathbf{u}_{\mathbf{i}} \rangle$ on the *i*th crack is

$$\langle \mathbf{u}_{\mathbf{i}} \rangle = A_1 \mathrm{e}^{ik_{\mathrm{p}}(x_1+p_1)\sin\theta + i\left(k_{\mathrm{p}}\cos\theta + \kappa\right)(x_2+p_2)} \left(\sin\theta, \cos\theta + \kappa_{\mathrm{r}}/k_{\mathrm{p}}\right). \tag{9}$$

The scattering wavefield by the *i*th crack can be obtained by the representation theorem (e.g. Kawahara & Yamashita 1992):

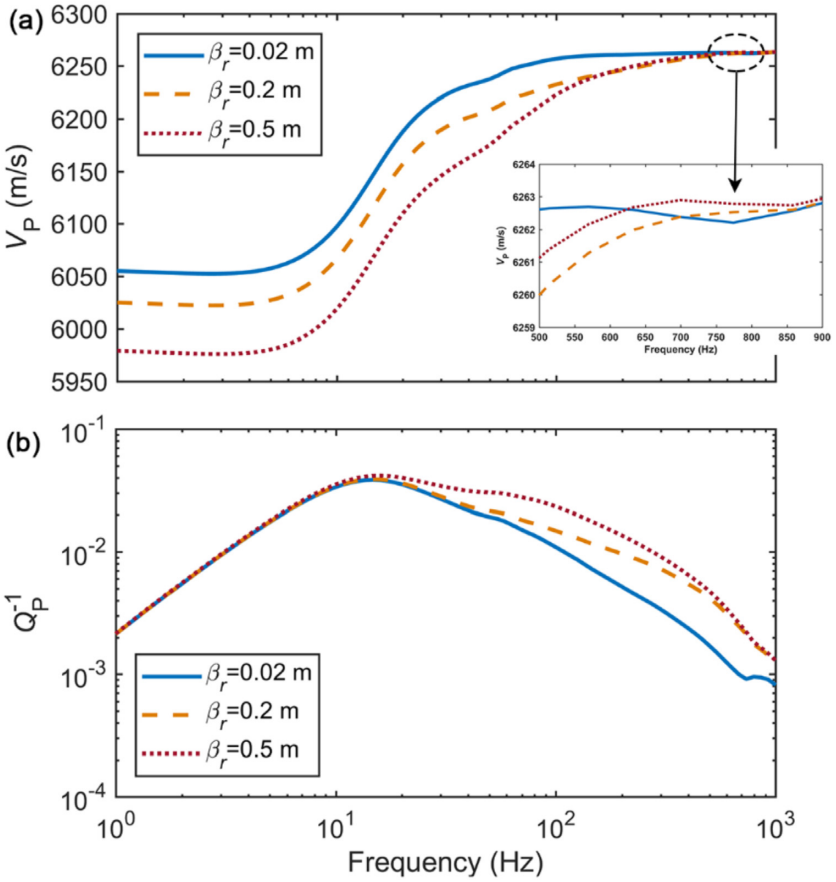

Figure 4. *P*-wave velocity (a) and dissipation factor (b) as a function of frequency for different crack thicknesses β_{r} at oblique incidence ($\theta = 45^{\circ}$).

$$[\mathbf{S_i}\,\langle \mathbf{u_i}\rangle]_j = -\int_{-a_{\mathrm{r}}}^{a_{\mathrm{r}}} [\Delta \mathbf{u_i}\,(\zeta_1, p_1, p_2)]_l \Gamma_{jl}\,(x_1, x_2|\zeta_1, 0)\,\mathrm{d}\zeta_1,\ \ j, l = 1, 2, \tag{10}$$

where $\Delta \mathbf{u_i}$ is the displacement discontinuity across the ith crack, and the stress tensor Γ_{jl} can be expressed as

$$\Gamma_{jl}\,(x_1, x_2|\zeta_1, \zeta_2) = \frac{i}{4}\left[\delta_{12}\left(1 - 2k_{\mathrm{p}}^2/k_{\mathrm{s}}^2\right)\frac{\partial}{\partial x_j}H_0^{(1)}\left(k_{\mathrm{p}}R\right) + \left(\delta_{jl}\frac{\partial}{\partial x_2} + \delta_{j2}\frac{\partial}{\partial x_l}\right)H_0^{(1)}\left(k_{\mathrm{s}}R\right)\right.$$
$$\left. -\frac{2}{k_{\mathrm{s}}^2}\frac{\partial^3}{\partial x_j \partial x_l \partial x_2}\left(H_0^{(1)}\left(k_{\mathrm{p}}R\right) - H_0^{(1)}\left(k_{\mathrm{s}}R\right)\right)\right], \tag{11}$$

where k_{s} is the S wavenumber, δ_{jl} is the Kronecker delta, $H_0^{(1)}(\cdot)$ is the first kind zeroth-order Hankel function, and $R^2 = (x_1 - \zeta_1)^2 + (x_2 - \zeta_2)^2$.

Then, the stress field σ_{jk}^E and σ_{jk}^S caused by $\langle \mathbf{u_i}\rangle$ and $\mathbf{S_i}\langle \mathbf{u_i}\rangle$ can be obtained according to Hooke's law (Timoshenko 1951) as (Kawahara & Yamashita 1992)

$$\sigma_{jk}^E = \lambda\delta_{jk}\frac{\partial}{\partial x_l}[\langle \mathbf{u_i}\rangle]_l + \mu\left(\frac{\partial}{\partial x_k}[\langle \mathbf{u_i}\rangle]_j + \frac{\partial}{\partial x_j}[\langle \mathbf{u_i}\rangle]_k\right),\ \ j, k, l = 1, 2, \tag{12}$$

$$\sigma_{jk}^S = \lambda\delta_{jk}\frac{\partial}{\partial x_l}[\mathbf{S_i}\,\langle \mathbf{u_i}\rangle]_l + \mu\left(\frac{\partial}{\partial x_k}[\mathbf{S_i}\,\langle \mathbf{u_i}\rangle]_j + \frac{\partial}{\partial x_j}[\mathbf{S_i}\,\langle \mathbf{u_i}\rangle]_k\right),\ \ j, k, l = 1, 2, \tag{13}$$

respectively, where λ and μ are the Lamé constants of the cracked media (Guo *et al.* 2018).

By substituting eqs (10) and (11) into eq. (13), we obtain

$$\sigma_{jk}^S = -\mu\int_{-a_{\mathrm{r}}}^{a_{\mathrm{r}}} [\Delta \mathbf{u_i}\,(\zeta_1, p_1, p_2)]_l T_{jkl}\,(x_1, x_2|\zeta_1, 0)\,\mathrm{d}\zeta_1, \tag{14}$$

where the T_{jkl} is given in Appendix B.

There is viscous friction between the fluid and crack surfaces (Kawahara & Yamashita 1992). The crack volume compression or extension and the viscous friction can cause normal and shear stresses, respectively. These are

$$\sigma_{12}^E + \sigma_{12}^S = -i\omega\eta\frac{[\Delta \mathbf{u_i}\,(x_1, p_1, p_2)]_1}{\beta_{\mathrm{r}}},\ |x_1| < a_{\mathrm{r}},\ x_2{=}0, \tag{15}$$

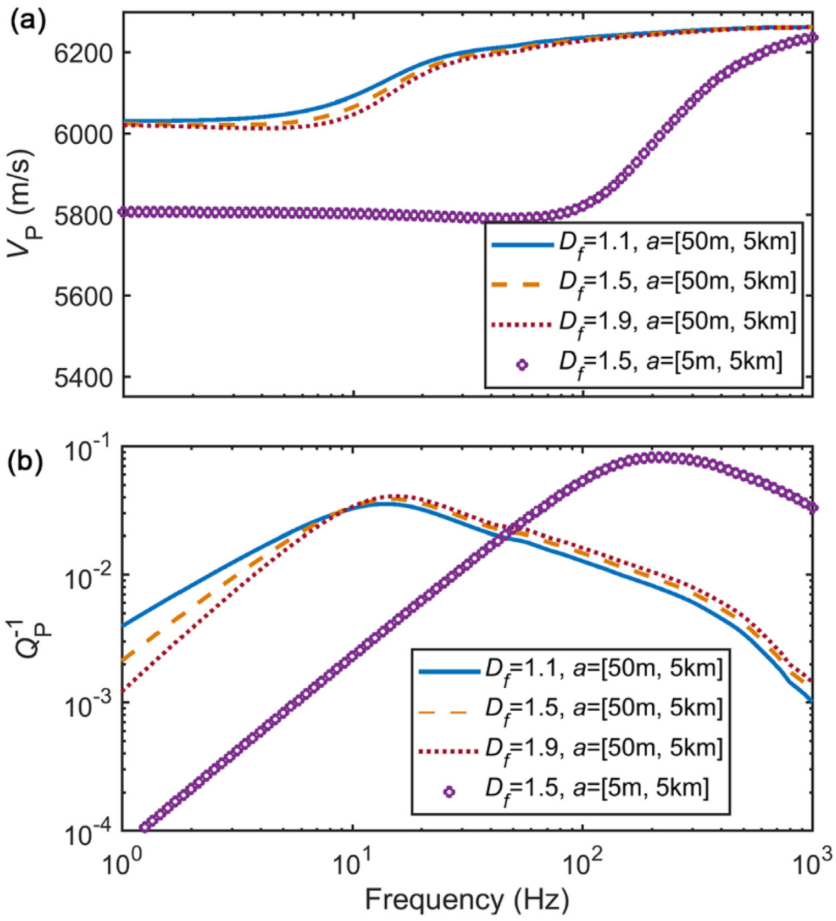

Figure 5. *P*-wave velocity (a) and dissipation factor (b) as a function of frequency for different fractal dimensions D_f and crack radius ranges at oblique incidence ($\theta = 45^\circ$).

$$\sigma_{22}^{E} + \sigma_{22}^{S} = K_f \frac{[\Delta \mathbf{u_i}(x_1, p_1, p_2)]_2}{\beta_r}, |x_1| < a_r, x_2{=}0, \tag{16}$$

where K_f and η are the bulk modulus and viscosity of the saturating fluid, respectively (Guo *et al.* 2018).

Substituting eqs (9), (12) and (14) into eqs (15) and (16) yields

$$\int_{-a_r}^{a_r} D_1(\zeta_1)\, T_{121}(x_1, 0|\zeta_1, 0)\, \mathrm{d}\zeta_1 - \mathrm{e}^{ik_p x_1 \sin\theta} = \frac{i\omega\eta}{\mu} \frac{D_1(x_1)}{\beta_r}, \ |x_1| < a_r, \tag{17}$$

$$\int_{-a_r}^{a_r} D_2(\zeta_1)\, T_{222}(x_1, 0|\zeta_1, 0)\, \mathrm{d}\zeta_1 - \mathrm{e}^{ik_p x_1 \sin\theta} = -\frac{K_f}{\mu} \frac{D_2(x_1)}{\beta_r}, \ |x_1| < a_r. \tag{18}$$

The normalized shear displacement discontinuities (D_1 and D_2) across the crack are given in Appendix A. Then, κ_r is determined by rewriting explicitly the right-hand side of eq. (6) through the representation theorem and the boundary conditions, and comparing it with the right-hand side of eq. (8),

$$\kappa_r{=}\varepsilon_r \hat{\phi}_1 \gamma k_p \sin 2\theta \sin\theta + \varepsilon_r \hat{\phi}_2 \frac{k_p}{2\gamma \cos\theta} \left(1 - 2\gamma \sin^2\theta\right)^2, \tag{19}$$

where $\gamma{=}V_S^2/V_P^2$, V_p, V_s are the *P*- and *S*-wave velocities, respectively, $\varepsilon_r{=}v_r a_r^2$ is the crack density for cracks with radius a_r, and $\hat{\phi}_1$ and $\hat{\phi}_2$ are given in Appendix A.

For cracks with radius range $[a_{min}, a_{max}]$, the total coefficient κ is

$$\kappa{=}\int_{a_{min}}^{a_{max}} \left(\varepsilon_r \hat{\phi}_1(a_r) \gamma k_p \sin 2\theta \sin\theta + \varepsilon_r \hat{\phi}_2(a_r) \frac{k_p}{2\gamma \cos\theta} \left(1 - 2\gamma \sin^2\theta\right)^2\right) \mathrm{d}a_r, \tag{20}$$

Thus, the *P*-wave phase velocity and attenuation can be obtained as (Kawahara & Yamashita 1992):

$$V_{pe} = V_p \left(1 - \frac{\cos\theta}{k_p} \mathrm{Re}\kappa\right), \tag{21}$$

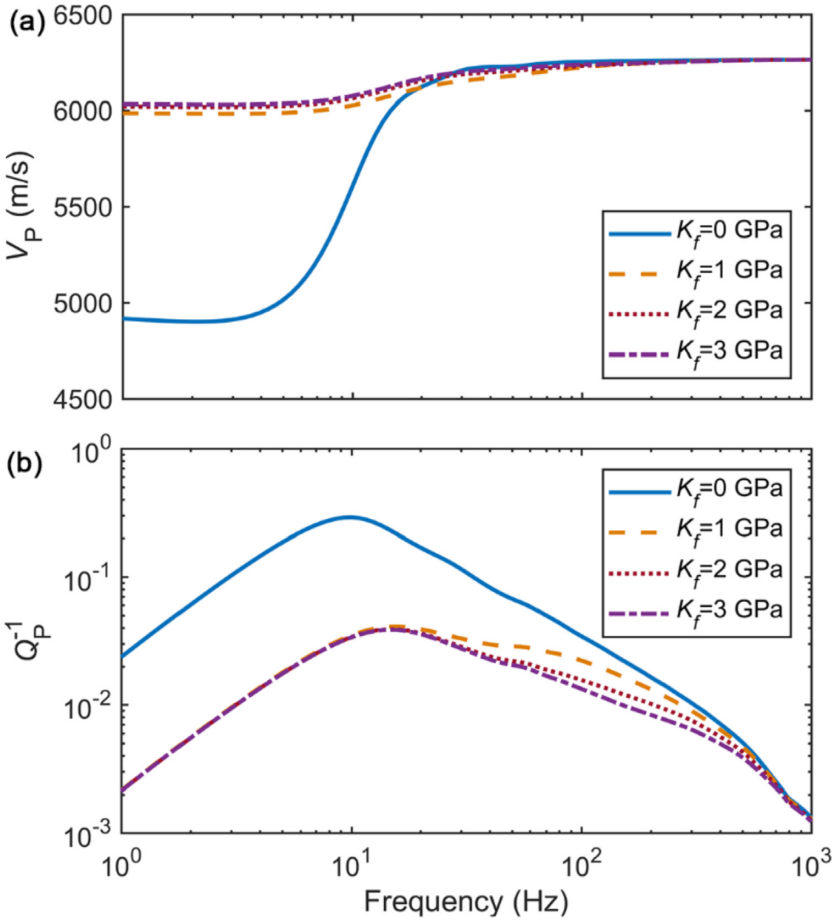

Figure 6. *P*-wave velocity (a) and dissipation factor (b) as a function of frequency for different fluid bulk moduli K_f at oblique incidence ($\theta = 45°$).

$$Q_p^{-1} = 2\frac{\cos\theta}{k_p}\mathrm{Im}\kappa, \tag{22}$$

respectively.

2.3 Partial saturation

Velocity dispersion and attenuation are affected by the pore fluid distribution, which has fractal characteristics evidenced from experiments and computational simulations (Berkowitz & Hansen 2001; Helle *et al.* 2003), and generally it is not so clear how those anelastic properties are related to the medium fractality. We assume that the cracks are saturated with two immiscible fluids, where one fluid saturates a crack length $2a_r s_w$ and the other a length $2a_r(1 - s_w)$, where s_w is the saturation of the first fluid. The displacement discontinuities across cracks saturated with different fluids can be calculated with the same derivations leading to eqs (17) and (18). Thus, coefficient κ can be obtained from eq. (20) as

$$\begin{aligned}\kappa = &\int_{a_{\min}s_w}^{a_{\max}s_w} \varepsilon_r\hat{\phi}_1(a_{r1})\gamma k_p \sin 2\theta \sin\theta + \varepsilon_r\hat{\phi}_2(a_{r1})\frac{k_p}{2\gamma\cos\theta}\left(1 - 2\gamma\sin^2\theta\right)^2 da_r \\ &+ \int_{a_{\min}(1-s_w)}^{a_{\max}(1-s_w)} \varepsilon_r\hat{\phi}_1(a_{r2})\gamma k_p \sin 2\theta \sin\theta + \varepsilon_r\hat{\phi}_2(a_{r2})\frac{k_p}{2\gamma\cos\theta}\left(1 - 2\gamma\sin^2\theta\right)^2 da_r,\end{aligned} \tag{23}$$

where $a_{r1}{=}a_r s_w$ and $a_{r2}{=}a_r(1 - s_w)$ are equivalent crack radii.

P-wave phase velocity and attenuation at partial saturation can be calculated by eqs. (21-23). The scattering at the fluid interfaces and the effect of wave-induced fluid flow are not considered.

3 EXAMPLE

An example illustrates the scattering attenuation (Q_p^{-1}) and velocity dispersion in rocks with self-similar (fractal) cracks. Most of the properties correspond to a carbonate reservoir with negligible stiff porosity (Guo *et al.* 2018). The bulk and shear moduli of the background medium are 63.7 GPa and 31.7 GPa, respectively, and the density is 2.70 g cm^{-3}, according to Mavko *et al.* (2009). Cracks with fractal dimension 1.5

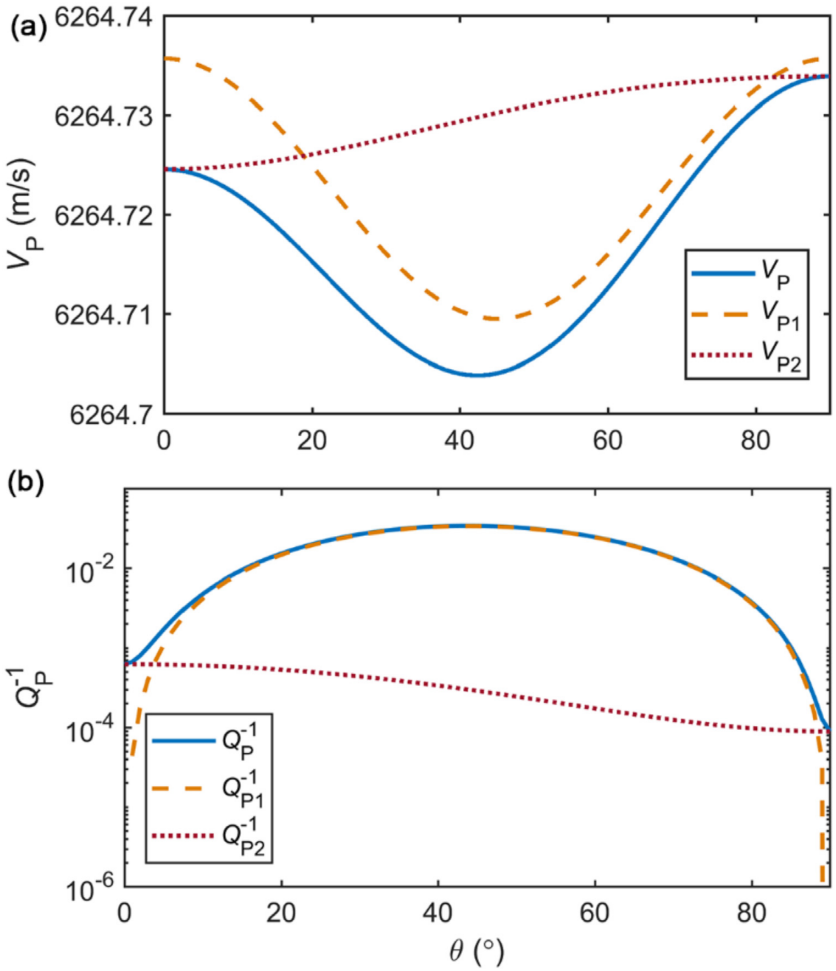

Figure 7. *P*-wave velocity (a) and dissipation factor (b) as a function of the incidence angle. The frequency is 10 Hz. The subscripts 1 and 2 denote the dispersion and attenuation related to the shear and normal crack displacement discontinuities, respectively.

and range [50 m, 5000 m] are assumed. The crack thickness is 0.2 m. The total crack density is 0.1 and that of each radius is determined from the probability density function eq. (4). The bulk modulus and viscosity of the saturating fluid are 2.25 GPa and 0.1 Pa s, respectively. The effects of the incidence angle, crack and fluid properties (i.e. crack thickness, crack density, and fluid bulk modulus) are analysed. When investigating the effect of a property (e.g. the fractal dimension), the other parameters are fixed.

3.1 Effect of the incidence angle

The frequency-dependent dispersion and attenuation (dissipation factor) as a function of the incidence angle θ are shown in Fig. 2, where we observe that the *P*-wave velocity increases with frequency (resonant or Mie scattering regime). The anelasticity is significant at intermediate incidence angles, where the characteristic frequency of the relaxation peak shifts to low frequencies. Q_p^{-1} at low and high frequencies is approximately proportional to f^2 and f^{-1}, respectively. Similar results are also observed by Yamashita (1990) and Guo *et al.* 2018).

3.2 Effects of crack density, thickness and fractal dimension

The results by varying one crack property are similar at different incidence angles. Thus, we only consider oblique incidence ($\theta = 45^\circ$). Fig. 3 illustrates the effect of crack density (ε). The dispersion and attenuation increase linearly with increasing crack density due to the Foldy approximation, which can be deduced from eqs (20)–(22) at first order in ε. The scattering characteristic frequency is independent of ε because the interaction between cracks is not considered due to the assumption of sparsely distributed cracks.

Fig. 4 shows the results as a function of frequency and different crack thicknesses (β_r). The *P*-wave velocity is significantly affected by β_r in the low-frequency band, and it decreases with increasing thickness, while an opposite behaviour is observed at high frequencies. This is because the dispersion increases more rapidly with crack thickness in the resonance scattering regime. Fig. 4(b) shows that Q_p^{-1} increases with thickness at high frequencies, due to the increasing normal crack displacement discontinuity. However, the effect of β_r is weaker at

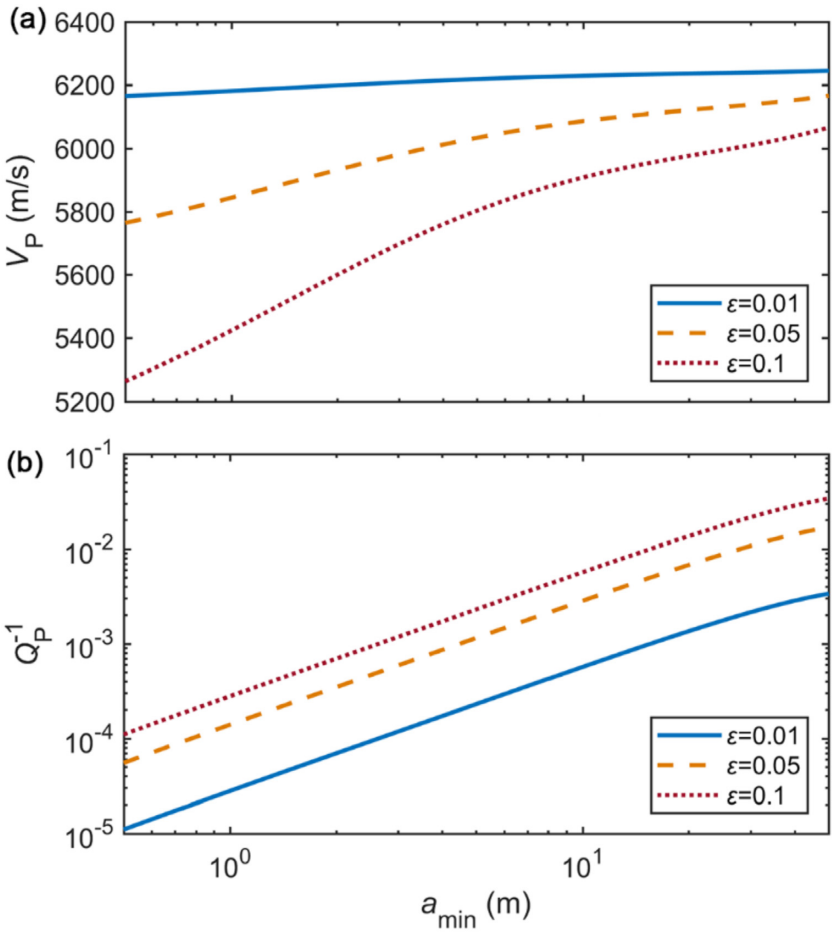

Figure 8. *P*-wave velocity (a) and dissipation factor (b) as a function of the smallest crack radius ($a_{\min}$) for different crack densities ε at $\theta = 45^\circ$. The frequency is 10 Hz and $a_{\max}$ is 5 km.

low frequencies because the attenuation is mainly caused by the shear displacement discontinuity at the cracks. The scattering characteristic frequency is almost the same.

Fig. 5 shows the effect of different fractal dimensions (D_f). A large D_f implies that the crack size distribution is more uniform (finely textured). *P*-wave velocity decreases when D_f increases in the resonance scattering regime for the same crack radius range. Q_p^{-1} decreases and increases at low and high frequencies, respectively, with increasing fractal dimension. The characteristic frequency moves to higher frequencies with D_f, because there are smaller cracks when D_f is higher. The effect of fractal dimension is weak when the interaction between cracks is not considered. We observed that changing the crack radius ranges from [50 m, 5000 m] to [5 m, 5000 m] with the same fractal dimension D_f, the characteristic frequency shifts to higher frequencies by one order of magnitude and the attenuation maximum also increases.

3.3 Effects of fluid bulk modulus and viscosity

Fig. 6 shows the effect of the fluid bulk modulus on attenuation. The velocity increases and decreases at low and high frequencies, respectively, with increasing K_f. Stronger velocity variations are observed for the case of a low bulk modulus, because the scattered field is enhanced by the increasing stiffness contrast between the cracks and background medium. *P*-wave dispersion and attenuation increase with decreasing K_f and have a maximum when K_f is zero (dry cracks). Moreover, the attenuation peak shifts toward lower frequencies when K_f decreases to zero. Similar results were obtained by Sabina *et al.* (1993), Smyshlyaev *et al.* (1993), Guo *et al.* (2018) and Song *et al.* (2019). Finally, the fluid viscosity (η) has no effect, because the shear displacement discontinuity is almost unaffected by η due to the small value of $(\omega\eta)/\mu$ in the right side of eq. (17). Similar results are also shown in Guo *et al.* (2018) and Song *et al.* (2019).

3.4 Effects of displacement discontinuity, crack radius range and fractal dimension

Fig. 7 shows the velocity and attenuation as a function of the incidence angle at 10 Hz. The scattering regime mainly regards 4–400 Hz. Q_{p1}^{-1} calculated from the shear discontinuity has a maximum at $\theta = 45^\circ$ due to shear stress caused by the viscous friction between the fluid and the crack surfaces. In contrast Q_{p2}^{-1} (normal discontinuity) decreases with θ because the normal stress induced by the crack volume compression

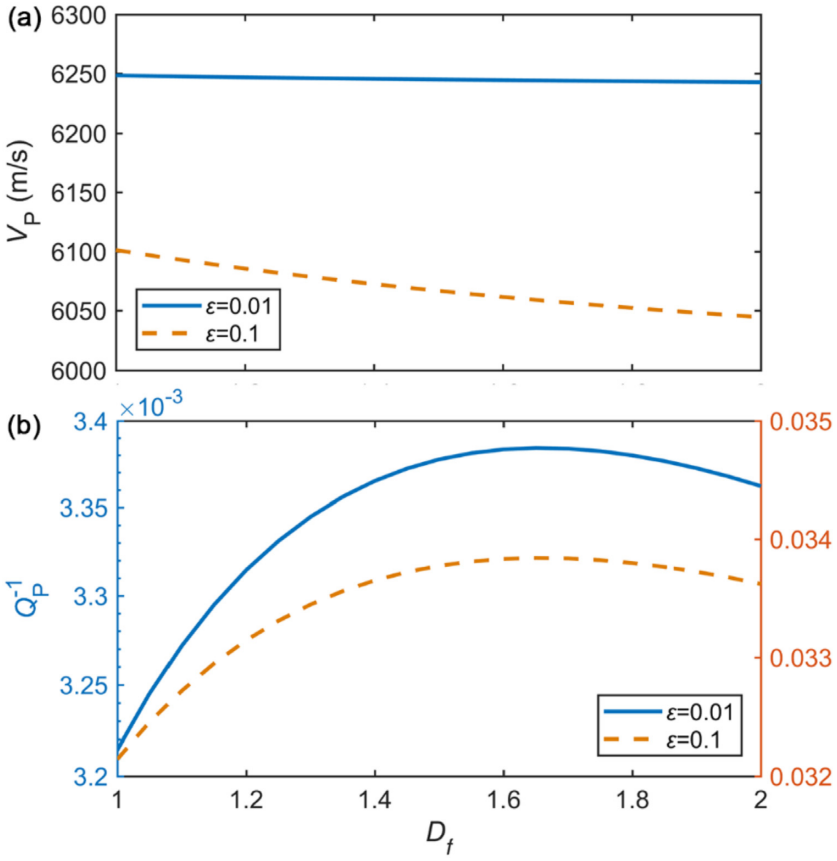

Figure 9. *P*-wave velocity (a) and dissipation factor (b) as a function of the fractal dimension D_f for different crack densities ε at $\theta = 45^\circ$. The frequency is 10 Hz.

decreases with θ. The total attenuation Q_p^{-1} is mainly affected by Q_{p1}^{-1}. Fig. 8 shows the effect of the smallest crack radius (a_{min}) at 10 Hz and $a_{max} = 5$ km. The *P*-wave velocity gradually increases with a_{min} while Q_p^{-1} is approximately proportional to a_{min} for different crack densities. Fig. 9 shows the results as a function of fractal dimension at 10 Hz. The *P*-wave velocity decreases approximately linearly when attenuation first increases and slightly decreases with the fractal dimension. The variation of Q_p^{-1} with D_f is much less than that with a_{min} when the velocity changes are of the same order of magnitude.

3.5 Effect of partial saturation

We consider a medium saturated with liquid and gas, whose bulk moduli are 1 and 3 GPa (liquid) and 0.1 GPa, respectively, and the corresponding viscosities are 1 cP and 0.03 cP, respectively. Fig. 10 shows the velocity and attenuation as a function of the liquid saturation at 10 Hz. As expected, the *P*-wave velocity mainly increases with saturation and attenuation has a minimum at approximately $s_w = 80$ per cent. Maximum attenuation occurs when the cracks are filled with a highly compressible fluid, such as gas. The variations of V_p and $Q_p^{-1}$with saturation are non-monotonous. For a partial saturation case, the crack space saturated with liquid decreases in comparison to the full liquid saturation case, resulting in the smaller radii of the effective liquid-saturated cracks. Thus, the variation of saturation may cause the shift of relaxation peak to different frequencies so as to effect on V_p and Q_p^{-1}. Whereas, the variation of the effective fluid bulk modulus, which corresponds to the saturation change, may also affect V_p and Q_p^{-1}. The variations of V_p and Q_p^{-1} are related to the both factors.

4 DISCUSSION

The frequency dependence of the *S*-wave attenuation in the Earth crust has been extensively studied from earthquakes at low frequencies (e.g. Aki 1980; Shapiro & Faizullin 1992; Sato *et al.* 2012), showing that the peak occurs at approximately 0.5 Hz (Matsunami 1988). This dependence can be used to determine the crack length distribution. For example, Yamashita (1990) estimated a maximum crack radius within the range [2.4, 4.4] km and a minimum one at [1.2, 1.8] km by assuming a shear wave velocity of 4 km s^{-1}. By considering the phase velocities and attenuation for an incident *S* wave, which can be derived in a similar manner to those of an incident *P* wave, the equations are

$$\kappa = \int_{a_{min}}^{a_{max}} \left(\varepsilon_r \hat{\phi}_1 (a_r) \frac{k_s}{2\cos\theta} (\cos 2\psi)^2 + \varepsilon_r \hat{\phi}_2 (a_r) k_s \sin 2\psi \sin\psi \right) da_r, \tag{24}$$

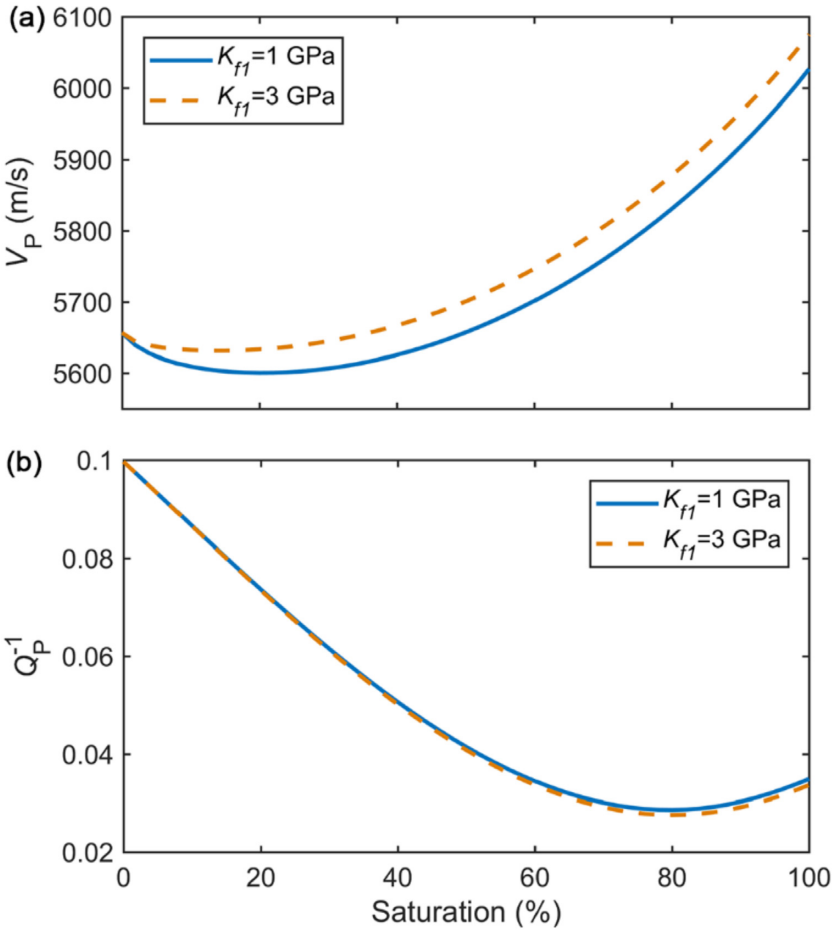

Figure 10. *P*-wave velocity (a) and dissipation factor (b) as a function of saturation for different fluid bulk moduli at $\theta = 45°$. The frequency is 10 Hz.

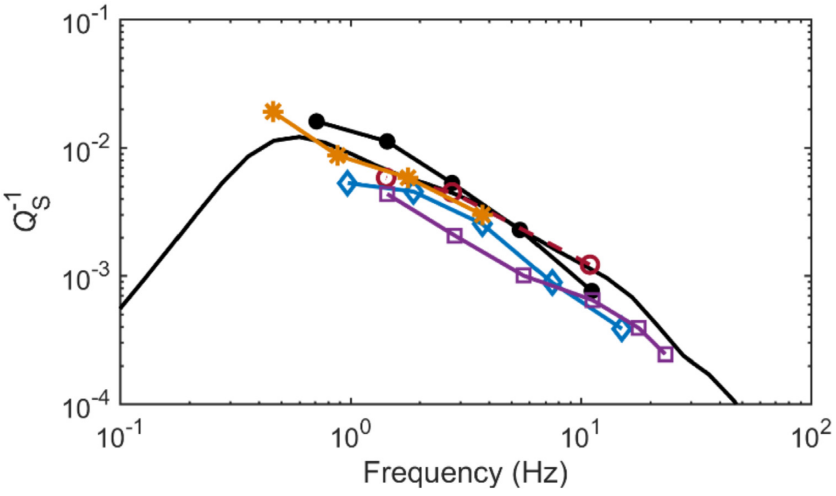

Figure 11. Simulated *S*-wave attenuation (solid line) as a function of frequency for a crack-radius range of [1.2, 4] km and attenuation values (symbols) from local earthquakes. The fractal dimension is 2.

$$V_{se} = V_s\left(1 - \frac{\cos\psi}{k_s}\mathrm{Re}\kappa\right), \tag{25}$$

$$Q_s^{-1} = 2\frac{\cos\psi}{k_s}\mathrm{Im}\kappa, \tag{26}$$

where ψ is given by Snell's law, $k_s \sin\psi = k_p \sin\theta$.

Fig. 11 shows the simulated frequency-dependent *S*-wave attenuation for $D_f = 2$ when the crack radius range is [1.2, 4] km and attenuation values (symbols) corresponding to local earthquakes obtained from their coda waves. The result shows that the frequency of the relaxation peak is 0.5 Hz, which well agrees with the seismological observations in different areas (Matsunami 1988). The crack sizes can be estimated when the fractal dimension has been determined.

5 CONCLUSIONS

We have studied *P*-wave scattering dispersion and attenuation in isotropic elastic media with a fractal (self-similar) size distribution of fluid-saturated aligned cracks. We assume that the cracks do not interact with each other. For each crack radii, the displacement discontinuities across the cracks are obtained by the Foldy approximation and the representation theorem based on boundary conditions. We show phase velocity and dissipation factor (reciprocal of the quality factor) as a function of the incidence angle, and crack and fluid properties. The results show that *P*-wave velocity decrease approximately linearly when the fractal dimension increases in the resonance scattering regime, and attenuation increases with crack density and thickness and decreases with the fluid bulk modulus. Attenuation is mainly caused by shear displacement discontinuities at oblique incidence angles and decreases with incidence angle only at high frequencies. Attenuation mainly increases when the crack is filled with a high-compressibility fluid. The location of the attenuation peak (or scattering characteristic frequency) moves to low frequencies at an oblique incident angle, and to high frequencies with increasing fractal dimension and fluid bulk modulus. The effect of fluid viscosity is negligible.

ACKNOWLEDGEMENTS

This work was supported by the Jiangsu Province Science Fund for Distinguished Young Scholars (BK20200021), the Fundamental Research Funds for the Central Universities (B210203039), the research funds from SINOPEC Key Laboratory of Geophysics, the Jiangsu Innovation and Entrepreneurship Plan, the National Natural Science Foundation of China (41974123), and the China Scholarship Council (201906710129).

DATA AVAILABILITY

The related data are accessible by contacting the corresponding author.

REFERENCES

Aki, K., 1980. Scattering and attenuation of shear waves in the lithosphere, *J. geophys. Res.,* **85,** 6496–6504.

Ba, J., Ma, R., Carcione, J.M. & Picotti, S., 2019. Ultrasonic wave attenuation dependence on saturation in tight oil siltstones, *J. Pet. Sci. Eng.,* **179,** 1114–1122.

Ba, J., Xu, W., Fu, L.-Y., Carcione, J.M. & Zhang, L., 2017. Rock anelasticity due to patchy saturation and fabric heterogeneity: a double double-porosity model of wave propagation, *J. geophys Res.,* **122,** 1949–1976.

Berkowitz, B. & Hansen, D.P., 2001. A numerical study of the distribution of water in partially saturated porous rock, *Transp. Porous Media,* **45,** 301–317.

Carcione, J. M., Picotti, S. & Santos, J.E., 2012. Numerical experiments of fracture-induced velocity and attenuation anisotropy, *Geophys. J. Int.,* **191,** 1179–1191.

Carcione, J.M., 2014. *Wave Fields in Real Media: Wave Propagation in Anisotropic, Anelastic Porous and Electromagnetic Media,* 3rd edn, Vols. 1–38, Elsevier Science.

Foldy, L.L., 1945. The multiple scattering of waves. I. General theory of isotropic scattering by randomly distributed scatterers, *Phys. Rev.,* **67,** 107–119.

Fu, B.-Y., Fu, L.-Y., Guo, J., Galvin, R.J. & Gurevich, B., 2020. Semi-analytical solution to the problem of frequency dependent anisotropy of porous media with an aligned set of slit cracks, *Int. J. Eng. Sci.,* **147,** 103209.

Fu, B.-Y., Guo, J., Fu, L.-Y., Glubokovskikh, S., Galvin, R.J. & Gurevich, B., 2018. Seismic dispersion and attenuation in saturated porous rock with aligned slit cracks, *J. geophys. Res.,* **123,** 6890–6910.

Garbin, H.D. & Knopoff, L., 1975. Elastic moduli of a medium with liquid-filled cracks, *Q. appl. Math.,* **33,** 301–303.

Giri, A., Tarafdar, S., Gouze, P. & Dutta, T., 2013. Fractal geometry of sedimentary rocks: simulation in 3-D using a relaxed bidisperse ballistic deposition model, *Geophys. J. Int.,* **192,** 1059–1069.

Guo, J., Gurevich, B. & Shuai, D., 2020. Frequency-dependent *P*-wave anisotropy due to scattering in rocks with aligned fractures, *Geophysics,* **85,** MR97–MR105.

Guo, J., Shuai, D., Wei, J., Ding, P. & Gurevich, B., 2018. *P*-wave dispersion and attenuation due to scattering by aligned fluid saturated fractures with finite thickness: theory and experiment, *Geophys. J. Int.,* **215,** 2114–2133.

Guo, M.-Q., Fu, L.-Y. & Ba, J., 2009. Comparison of stress-associated coda attenuation and intrinsic attenuation from ultrasonic measurements, *Geophys. J. Int.,* **178,** 447–456.

Gurevich, B., Sadovnichaja, A.P., Lopatnikov, S.L. & Shapiro, S.A., 1998. Scattering of a compressional wave in a poroelastic medium by an ellipsoidal inclusion, *Geophys. J. Int.,* **133,** 91–103.

Helle, H.B., Pham, N.H. & Carcione, J.M., 2003. Velocity and attenuation in partially saturated rocks: poroelastic numerical experiments, *Geophys. Prospect,* **51,** 551–566.

Hudson, J.A., 1980. Overall properties of a cracked solid, *Math. Proc. Camb. Phil. Soc.,* **88,** 371–384.

Hudson, J.A., 1981. Wave speeds and attenuation of elastic waves in material containing cracks, *Geophys. J. Int.,* **64,** 133–150.

Hudson, J.A., 1986. A higher order approximation to the wave propagation constants for a cracked solid, *Geophys. J. Int.,* **87,** 265–274.

Katz, null & Thompson, null., 1985. Fractal sandstone pores: implications for conductivity and pore formation, *Phys. Rev. Lett.,* **54,** 1325–1328.

Kawahara, J., 1992. Scattering of *P*, *SV* waves by random distribution of aligned open cracks, *J. Phys. Earth,* **40,** 517–524.

Kawahara, J. & Yamashita, T., 1992. Scattering of elastic waves by a fracture zone containing randomly distributed cracks, *Pure appl. Geophys.,* **139,** 121–144.

Keogh, P.S., 1986. High-frequency scattering of a normally incident plane compressional wave by a penny-shaped crack, *Q. J. Mech. Appl. Math.,* **39,** 535–566.

Krenk, S., Schmidt, H. & Ursell, F.J., 1982. Elastic wave scattering by a circular crack, *Phil. Trans. R. Soc. Lond., A,* **308,** 167–198.

Krohn, C.E., 1988a. Fractal measurements of sandstones, shales, and carbonates, *J. geophys. Res.,* **93,** 3297–3305.
Krohn, C.E., 1988b. Sandstone fractal and Euclidean pore volume distributions, *J. geophys. Res.,* **93,** 3286–3296.
Lerche, I., 1985. Multiple scattering of seismic waves in fractured media: crosscorrelation as a probe of fracture intensity, *Pure appl. Geophys.,* **123,** 503–542.
Lerche, Ian & Petroy, D., 1986. Multiple scattering of seismic waves in fractured media: velocity and effective attenuation of the coherent components of *P* waves and *S* waves, *Pure appl. Geophys.,* **124,** 975–1019.
Ma, R. & Ba, J., 2020. Coda and intrinsic attenuations from ultrasonic measurements in tight siltstones, *J. geophys. Res.,* **125,** doi:10.1029/2019JB018825.
Mal, A.K., 1970. Interaction of elastic waves with a penny-shaped crack, *Int. J. Eng. Sci.,* **8,** 381–388.
Martin, P.A. & Ursell, F.J., 1981. Diffraction of elastic waves by a penny-shaped crack, *Proc. R. Soc. A,* **378,** 263–285.
Matsunami, K., 1988. Laboratory measurements of elastic wave attenuation by scattering due to random heterogeneities, *Bull. Disaster Prevention Res. Inst.,* **38,** 1–16.
Mavko, G., Mukerji, T. & Dvorkin, J., 2009. *The Rock Physics Handbook: Tools for Seismic Analysis of Porous Media,* 2nd edn, Cambridge Univ. Press.
Murai, Y., 2007. Scattering attenuation, dispersion and reflection of *SH* waves in two-dimensional elastic media with densely distributed cracks, *Geophys. J. Int.,* **168,** 211–223.
Murai, Y., Kawahara, J. & Yamashita, T., 1995. Multiple scattering of *SH* waves in 2-D elastic media with distributed cracks, *Geophys. J. Int.,* **122,** 925–937.
Pang, M., Ba, J., Carcione, J.M., Picotti, S., Zhou, J. & Jiang, R., 2019. Estimation of porosity and fluid saturation in carbonates from rock-physics templates based on seismic *Q*, *Geophysics,* **84,** M25–M36.
Picotti, S., Carcione, J.M. & Ba, J., 2018. Rock-physics templates based on seismic *Q*, *Geophysics,* **84,** MR13–MR23.
Pulli, J.J., 1984. Attenuation of coda waves in New England, *Bull. seism. Soc. Am.,* **74,** 1149–1166.
Sabina, F.J., Smyshlyaev, V.P. & Willis, J.R., 1993. Self-consistent analysis of waves in a matrix-inclusion composite—I. Aligned spheroidal inclusions, *J. Mech. Phys. Solids,* **41,** 1573–1588.
Sato, H., Fehler, M.C. & Maeda, T., 2012. *Seismic Wave Propagation and Scattering in the Heterogeneous Earth,* 2nd edn, Springer.
Shapiro, S.A. & Faizullin, I.S., 1992. Fractal properties of fault systems by scattering of body seismic waves, *Tectonophysics,* **202,** 177–181.
Smyshlyaev, V.P., Willis, J.R. & Sabina, F.J., 1993. Self-consistent analysis of waves in a matrix-inclusion composite—II. Randomly oriented spheroidal inclusions, *J. Mech. Phys. Solids,* **41,** 1589–1598.
Song, Y., Hu, H. & Han, B., 2019. Elastic wave scattering by a fluid-saturated circular crack and effective properties of a solid with a sparse distribution of aligned cracks, *J. acoust. Soc. Am.,* **146,** 470, doi:10.1121/1.5116917.
Takahashi, T., Obana, K., Yamamoto, Y., Nakanishi, A., Kodaira, S. & Kaneda, Y., 2014. *S* wave attenuation structure on the western side of the Nankai subduction zone: implications for fluid distribution and dynamics, *J. geophys. Res.,* **119,** 7805–7822.
Timoshenko, S., 1951. *Theory of Elasticity,* McGraw-Hill. Retrieved from http://openlibrary.org/books/OL6090054M.
Vlastos, S., Liu, E., Main, I.G. & Narteau, C., 2007. Numerical simulation of wave propagation in 2-D fractured media: scattering attenuation at different stages of the growth of a fracture population, *Geophys. J. Int.,* **171,** 865–880.
Wu, R.-S. & Aki, K., 1985b. The fractal nature of the inhomogeneities in the lithosphere evidenced from seismic wave scattering, *Pure appl. Geophys.,* **123,** 805–818.
Wu, R.-S. & Aki, K., 1988. Multiple scattering and energy transfer of seismic waves—separation of scattering effect from intrinsic attenuation II. Application of the theory to Hindu Kush region, in *Scattering and Attenuations of Seismic Waves, Part I. Pageoph Topical Volumes,* pp. 49–80, eds Aki, K. & Wu, R.-S., Birkhäuser.
Wu, R. & Aki, K., 1985a. Scattering characteristics of elastic waves by an elastic heterogeneity, *Geophysics,* **50,** 582–595.
Yamashita, T., 1990. Attenuation and dispersion of *SH* waves due to scattering by randomly distributed cracks, *Pure appl. Geophys.,* **132,** 545–568.
Yu, B., Lee, L.J. & Cao, H., 2001. Fractal characters of pore microstructures of textile fabrics, *Fractals,* **9,** 155–163.
Yu, B. & Li, J., 2001. Some fractal characters of porous media, *Fractals,* **9,** 365–372.
Zhang, Ch. & Achenbach, J.D., 1991. Effective wave velocity and attenuation in a material with distributed penny-shaped cracks, *Int. J. Solids Struct.,* **27,** 751–767.
Zhang, Ch. & Gross, D., 1993a. Wave attenuation and dispersion in randomly cracked solids—I. Slit cracks, *Int. J. Eng. Sci.,* **31,** 841–858.
Zhang, Ch. & Gross, D., 1993b. Wave attenuation and dispersion in randomly cracked solids—II. Penny-shaped cracks, *Int. J. Eng. Sci.,* **31,** 859–872.
Zhang, L., Ba, J.,Carcione, J.M.& Fu, L.-Y.,2020. Differential poroelasticity model for wave dissipation in self-similar rocks, *Int. J. Rock Mech. Min. Sci.,* **128,** 104281.

SOLUTION OF EQS (17) AND (18)

Eqs (17) and (18) can be first normalized by the method of Kawahara & Yamashita (1992):

$$\int_{-1}^{1} \hat{D}_1\left(\hat{\xi}_1\right) \hat{T}_{121}\left(s, 0|\hat{\xi}_1, 0\right) \mathrm{d}\hat{\xi}_1 - \mathrm{e}^{i\hat{k}_\mathrm{p} s \sin\theta} = \frac{i\omega\eta a_\mathrm{r}}{\mu} \frac{\hat{D}_1(s)}{\beta_\mathrm{r}}, \ |s| < 1, \tag{A1}$$

$$\int_{-1}^{1} \hat{D}_2\left(\hat{\xi}_1\right) \hat{T}_{222}\left(s, 0|\hat{\xi}_1, 0\right) \mathrm{d}\hat{\xi}_1 - \mathrm{e}^{i\hat{k}_\mathrm{p} s \sin\theta} = \frac{K_\mathrm{f} a_\mathrm{r}}{\mu} \frac{\hat{D}_2(s)}{\beta_\mathrm{r}}, \ |s| < 1, \tag{A2}$$

where $\hat{\xi}_1, s, \hat{k}_\mathrm{p}, \hat{D}_1, \hat{D}_2, \hat{T}_{121}$ and $\hat{T}_{222}$ are the normalized values by half of the crack length as

$$\begin{aligned}
&\hat{\xi}_1 = \zeta_1 / a_\mathrm{r}, \\
&s = x_1 / a_\mathrm{r}, \\
&\hat{k}_\mathrm{p} = k_\mathrm{p} / a_\mathrm{r}, \\
&\hat{D}_1 = D_1 / a_\mathrm{r}, \\
&\hat{D}_2 = D_2 / a_\mathrm{r}, \\
&\hat{T}_{121} = a_\mathrm{r}^2 T_{121}, \\
&\hat{T}_{222} = a_\mathrm{r}^2 T_{222},
\end{aligned} \tag{A3}$$

where

$$D_1 = \frac{[\Delta \mathbf{u_i}(x_1, p_1, p_2)]_1}{2i\left(k_\mathrm{p}\cos\theta + \kappa_\mathrm{r}\right) \sin\theta A_1 \mathrm{e}^{ik_\mathrm{p} p_1 \sin\theta + i\left(k_\mathrm{p}\cos\theta + \kappa_\mathrm{r}\right) p_2}}, \tag{A4}$$

$$D_2 = \frac{[\Delta \mathbf{u_i}(x_1, p_1, p_2)]_2}{ik_\mathrm{p} A_1 \mathrm{e}^{ik_\mathrm{p} p_1 \sin\theta + i(k_\mathrm{p}\cos\theta + \kappa_\mathrm{r})p_2}\left[\left(k_\mathrm{s}^2/k_\mathrm{p}^2 - 2\right)\sin^2\theta + k_\mathrm{s}^2/k_\mathrm{p}^2\left(\cos\theta + \kappa_\mathrm{r}/k_\mathrm{p}\right)^2\right]}. \tag{A5}$$

Thus, eqs (A1) and (A2) can be discretized as

$$\sum_{n=1}^{M-1}\left(T_{mn}^{121} - \delta_{mn}\frac{i\omega\eta a_\mathrm{r}}{\mu\beta_\mathrm{r}}\right)\hat{D}_{1n} = \mathrm{e}^{i\hat{k}_\mathrm{p} s_m \sin\theta},\ m = 1, ..., M-1, \tag{A6}$$

$$\sum_{n=1}^{M-1}\left(T_{mn}^{222} + \delta_{mn}\frac{K_\mathrm{f} a_\mathrm{r}}{\mu\beta_\mathrm{r}}\right)\hat{D}_{2n} = \mathrm{e}^{i\hat{k}_\mathrm{p} s_m \sin\theta},\ m = 1, ..., M-1, \tag{A7}$$

where

$$\begin{aligned} &s_m = -1 + m\Delta s,\\ &\Delta s = 2/M,\\ &T_{mn}^{121} = \textstyle\int_{s_n-\Delta s/2}^{s_n+\Delta s/2}\hat{T}_{121}\left(s_m, 0|\hat{\xi}_1, 0\right)\mathrm{d}\hat{\xi}_1,\\ &T_{mn}^{222} = \textstyle\int_{s_n-\Delta s/2}^{s_n+\Delta s/2}\hat{T}_{222}\left(s_m, 0|\hat{\xi}_1, 0\right)\mathrm{d}\hat{\xi}_1. \end{aligned} \tag{A8}$$

The parameters T_{mn}^{121} and T_{mn}^{222} are given in Appendix B. Thus, $\hat{D}_1$ and $\hat{D}_2$ can be obtained from eqs (A6) and (A7). Then ϕ_1 and ϕ_2 can be calculated by

$$\phi_j = a_\mathrm{r}^2\hat{\phi}_j,\ j = 1, 2, \tag{A9}$$

where

$$\hat{\phi}_j = \sum_{m=1}^{M-1}\hat{D}_{1m}\mathrm{e}^{-i\hat{k}_\mathrm{p} s_m \sin\theta}\Delta s,\ j = 1, 2. \tag{A10}$$

EXPRESSIONS FOR T_{mn}^{121} AND T_{mn}^{222}

Kawahara & Yamashita (1992) give the equations. When $m = n$,

$$\begin{aligned} T_{nn}^{121} = &-\frac{\hat{k}_\mathrm{p}^2 - \hat{k}_\mathrm{s}^2}{\hat{k}_\mathrm{s}^2}\frac{4}{\pi\Delta s} - \frac{\hat{k}_\mathrm{p}^4 - \hat{k}_\mathrm{s}^4}{\hat{k}_\mathrm{s}^2}\frac{i\Delta s}{8}\\ &+\frac{\Delta s}{4\pi\hat{k}_\mathrm{s}^2}\left[\hat{k}_\mathrm{p}^4\log\frac{\hat{k}_\mathrm{p}\Delta s}{4} + \hat{k}_\mathrm{s}^4\log\frac{\hat{k}_\mathrm{s}\Delta s}{4} + \hat{k}_\mathrm{p}^4(C - 3/4) + \hat{k}_\mathrm{s}^4(C - 5/4)\right], \end{aligned} \tag{B1}$$

$$\begin{aligned} T_{nn}^{222} = &-\frac{\hat{k}_\mathrm{p}^2 - \hat{k}_\mathrm{s}^2}{\hat{k}_\mathrm{s}^2}\frac{4}{\pi\Delta s} - \frac{3\hat{k}_\mathrm{p}^4 - 4\hat{k}_\mathrm{p}^2\hat{k}_\mathrm{s}^2 + 3\hat{k}_\mathrm{s}^4}{\hat{k}_\mathrm{s}^2}\frac{i\Delta s}{8}\\ &+\frac{\Delta s}{4\pi\hat{k}_\mathrm{s}^2}\left[3\hat{k}_\mathrm{p}^4\log\frac{\hat{k}_\mathrm{p}\Delta s}{4} - 4\hat{k}_\mathrm{p}^2\hat{k}_\mathrm{s}^2\log\frac{\hat{k}_\mathrm{p}\Delta s}{4} + 3\hat{k}_\mathrm{s}^4\log\frac{\hat{k}_\mathrm{s}\Delta s}{4} + 2\hat{k}_\mathrm{s}^4\log\frac{\hat{k}_\mathrm{p}}{\hat{k}_\mathrm{s}}\right.\\ &\left.+\hat{k}_\mathrm{p}^2\hat{k}_\mathrm{s}^2(4C + 2) + \hat{k}_\mathrm{p}^4(3C - 5/4) + \hat{k}_\mathrm{s}^4(3C - 11/4)\right], \end{aligned} \tag{B2}$$

$$T_{nn}^{122} = T_{nn}^{221} = 0. \tag{B3}$$

When $m \neq n$,

$$\begin{aligned} T_{mn}^{121} = &-\frac{i}{4}\hat{k}_\mathrm{s}^2\Delta s H_0^{(1)}\left(\hat{k}_\mathrm{s} s_{mn}\right) - \frac{i\Delta s}{\hat{k}_\mathrm{s}^2}\left[\frac{1}{s_{mn}}\left\{\hat{k}_\mathrm{p}^3 H_1^{(1)}\left(\hat{k}_\mathrm{p} s_{mn}\right) - \hat{k}_\mathrm{s}^3 H_1^{(1)}\left(\hat{k}_\mathrm{s} s_{mn}\right)\right\}\right.\\ &\left.+\frac{3}{s_{mn}^2}\left\{\hat{k}_\mathrm{p}^3 H_0^{(1)}\left(\hat{k}_\mathrm{p} s_{mn}\right) - \hat{k}_\mathrm{s}^3 H_0^{(1)}\left(\hat{k}_\mathrm{s} s_{mn}\right)\right\} - \frac{6}{s_{mn}^3}\left\{\hat{k}_\mathrm{p} H_1^{(1)}\left(\hat{k}_\mathrm{p} s_{mn}\right) - \hat{k}_\mathrm{s} H_1^{(1)}\left(\hat{k}_\mathrm{s} s_{mn}\right)\right\}\right]\\ &-\frac{\hat{k}_\mathrm{p}^4 + \hat{k}_\mathrm{s}^4}{4\pi\hat{k}_\mathrm{s}^2}\left[\Delta s\log s_{mn} - \int_{s_n-\Delta s/2}^{s_n+\Delta s/2}\log\left|s_m - \hat{\xi}_1\right|\mathrm{d}\hat{\xi}_1\right] - \frac{\hat{k}_\mathrm{p}^2 - \hat{k}_\mathrm{s}^2}{\pi\hat{k}_\mathrm{s}^2}\left[\frac{\Delta s}{s_{mn}^2} - \int_{s_n-\Delta s/2}^{s_n+\Delta s/2}\frac{\mathrm{d}\hat{\xi}_1}{\left(s_m - \hat{\xi}_1\right)^2}\right], \end{aligned} \tag{B4}$$

$$
\begin{aligned}
T_{mn}^{222} = & -\frac{i}{4}\hat{k}_{\mathrm{s}}^2\left(1-2\frac{\hat{k}_{\mathrm{p}}^2}{\hat{k}_{\mathrm{s}}^2}\right)^2 \Delta s H_0^{(1)}\left(\hat{k}_{\mathrm{s}} s_{mn}\right) - \frac{i\Delta s}{\hat{k}_{\mathrm{s}}^2}\left[\frac{\hat{k}_{\mathrm{s}}^2}{s_{mn}}\left\{\hat{k}_{\mathrm{p}}\left(1-2\frac{\hat{k}_{\mathrm{p}}^2}{\hat{k}_{\mathrm{s}}^2}\right)H_1^{(1)}\left(\hat{k}_{\mathrm{p}} s_{mn}\right)+\hat{k}_{\mathrm{s}} H_1^{(1)}\left(\hat{k}_{\mathrm{s}} s_{mn}\right)\right\}\right. \\
& \left. -\frac{3}{s_{mn}^2}\left\{\hat{k}_{\mathrm{p}}^2 H_0^{(1)}\left(\hat{k}_{\mathrm{p}} s_{mn}\right)-\hat{k}_{\mathrm{s}}^2 H_0^{(1)}\left(\hat{k}_{\mathrm{s}} s_{mn}\right)\right\}+\frac{6}{s_{mn}^3}\left\{\hat{k}_{\mathrm{p}} H_1^{(1)}\left(\hat{k}_{\mathrm{p}} s_{mn}\right)-\hat{k}_{\mathrm{s}} H_1^{(1)}\left(\hat{k}_{\mathrm{s}} s_{mn}\right)\right\}\right] \\
& -\frac{3\hat{k}_{\mathrm{p}}^4-4\hat{k}_{\mathrm{p}}^2\hat{k}_{\mathrm{s}}^2+3\hat{k}_{\mathrm{s}}^4}{4\pi\hat{k}_{\mathrm{s}}^2}\left[\Delta s \log s_{mn}-\int_{s_n-\Delta s/2}^{s_n+\Delta s/2}\log\left|s_m-\hat{\zeta}_1\right|\mathrm{d}\hat{\zeta}_1\right] \\
& -\frac{\hat{k}_{\mathrm{p}}^2-\hat{k}_{\mathrm{s}}^2}{\pi\hat{k}_{\mathrm{s}}^2}\left[\frac{\Delta s}{s_{mn}^2}-\int_{s_n-\Delta s/2}^{s_n+\Delta s/2}\frac{\mathrm{d}\hat{\zeta}_1}{\left(s_m-\hat{\zeta}_1\right)^2}\right],
\end{aligned}
\tag{B5}
$$

$$
T_{mn}^{122} = T_{mn}^{221} = 0, \tag{B6}
$$

where $H_1^{(1)}(\cdot)$ is the first kind first-order Hankel function, $\hat{k}_{\mathrm{s}} = k_{\mathrm{s}}/a_{\mathrm{r}}$ is the normalized S-wave wavenumber, C is Euler's constant, $s_{mn} = |s_m - s_m|$ when $s_m = -1 + m\Delta s$ and $s_n = -1 + n\Delta s$. Eqs (B3) and (B6) mean

$$
T_{122}\left(x_1, 0|\zeta_1, 0\right) = T_{221}\left(x_1, 0|\zeta_1, 0\right) = 0. \tag{B7}
$$